High-Accuracy Localization and Calibration for 5-DoF Indoor Magnetic Positioning Systems

Markus Hehn , *Student Member, IEEE*, Erik Sippel, Christian Carlowitz, *Member, IEEE*, and Martin Vossiek, *Fellow, IEEE*

Abstract— **Magnetic local positioning systems are a well-suited candidate for reliable indoor positioning systems, as they are robust against blocking by dielectric materials like walls or people. The system presented in this paper is implemented with a one-axis magnetic transmitter and several three-axis field sensors connected to a complete sensor network. Unfortunately, the performance of the system is severely impaired by field sensor nonidealities such as magnetic coupling of the sensor coils, coil misalignment, field sensor rotation, and unsynchronized sampling. In this paper, the overall field sensor impairments and an additive Gaussian noise model superposing the magnetic field are mathematically described. Then, a novel calibration scheme for the overall field sensor nonidealities is presented. Furthermore, a statistically optimal localization procedure coping with the field sensor nonidealities is developed. The proposed novel localization and calibration algorithms are demonstrated in a common office environment with a size of 7 m × 5 m × 3 m. Thereby, the calibration impressively reduces the position root-mean-square error (RMSE) from 46.8 to 10.6 cm and the angle RMSE from 24.8° to 6.1°.**

Index Terms— **Calibration, field sensor, indoor navigation, localization, magnetic fields, magnetic local positioning.**

I. INTRODUCTION

CURRENTLY, local positioning systems are an important key technology. They contribute significantly to the expansion of the economy, improvement in security, and increase in productivity. Examples of applications are localization and coordination of robots, items, humans, and animals within buildings, information systems in museums and schools, assistance systems in hospitals, industrial automation, item tracking, virtual reality and augmented reality, and supporting firefighters, rescue, and safety personnel [1]–[3].

Various system concepts for local positioning systems have been developed and researched in recent years [1]–[3]. In principle, they can be divided into wave-, field-, and motion-based systems.

Existing wave-based systems are RF positioning systems [2], [3], acoustic systems with ultrasound [4],

and optical systems based on cameras [5], and other optical sensors like laserscanners [6]. Examples for RF positioning systems are narrowband RF systems that used WLAN [7], Zigbee [8], and Bluetooth [9], ultra-wideband systems (UWB) such as pulse radar [10], cellular-based systems [11], and radio-frequency identification (RFID [12]. Basically, they all attempt to estimate the target's position by processing a wave that was emitted from or reflected by the target. Typical measurement principles are time of flight, angle of arrival, and received signal strength [2]. For an acceptable position accuracy, the signal should be received via the line of sight (LoS). Hence, they are normally susceptible to multipath, fading and in-band interference, which in the worst case can lead to ambiguous or falsified position results.

Motion-based systems measure movement and calculate position based on this data. Examples are odometry [13] and inertial navigation systems (INSs), which utilize an inertial measurement unit (IMU) [14]. An IMU measures the acceleration and rotation rate with respect to an inertial system. The position can be calculated with double integration of the acceleration values. During the past few years, cheap and small IMUs in chip form based on microelectromechanical systems have become available. Unfortunately, degradation of sensor values leads to large position errors after a short time, as long as there is no online estimation of the sensor errors [15].

Field-based positioning systems estimate the target's position via a system model based on the electromagnetic field distribution. In the case of indoor localization, the magnetic field outperforms the electric field, as it is barely distorted by dielectric materials such as walls and groups of people [3], [16]. In principle, magnetic local positioning systems (MLPSs) can be divided into earth's magnetic field-based and artificial magnetic field-based systems [3].

The first group commonly uses fingerprint techniques, in which a map of earth's magnetic field distortion is stored [17]. Based on this data, the localization is accomplished. Earth's magnetic field-based systems have a high operating area [3] but are vulnerable to changes in the surrounding environment. The modified setting leads to a different set of measured values at the same reference points and, therefore, causes false estimated positions.

In [3], the second group is further subdivided into dc field-based and ac field-based systems. dc field-based systems can be found in [18] and [19]. Magnetic field-based location systems are robust against multipath, fading, and shading by

nonmetal materials [3]. Hence, they are well-suited for indoor localization. Moreover, they have a lower hardware complexity as microwave and RF-based systems [3]. Thereby, merging MLPS with other technologies as GPS [20] or INS [21], [22] facilitates robust localization. However, as the magnetic fields amplitude decreases cubically with distance in the near field, the range in LoS scenarios is smaller compared to wave-based systems [3]. By exploiting resonance effects, the range of ac field-based systems can increase compared to dc field-based systems [3].

Various ac field-based systems with different system topologies and algorithms were proposed in previous works, see [3] for an overview of existing systems and their performance. Generally, the systems either utilize one-axis coils [23]–[27] or three-axis coils [21], [22], [28]–[31] to detect the magnetic field. On the one hand, the use of three-axis sensors maximizes the information generated at each measurement point by measuring each dimension of the magnetic field. On the other hand, a variety of imperfections such as coupling, coil misalignment, field sensor rotation, amplitude, and phase errors caused by the analog circuits and signal processing, and unsynchronized sampling instances, degrade the localization performance. These imperfections represent the main challenge of current magnetic localization systems, see [31]. Hence, a corresponding calibration and localization scheme is necessary in order to improve the performance and increase the reliability of magnetic positioning systems.

For this purpose, we developed a mathematical description of the sensor effects. Furthermore, a novel robust calibration scheme is proposed in order to cope with the field sensors nonidealities. In addition, a 5-DoF localization algorithm for position and orientation estimation is developed, which incorporates the calibration result. The novel proposed calibration scheme impressively decreases localization-error from 46.8 to 10.6 cm and orientation-error from 24.8° to 6.1° in an office-room scenario. MLPS, designated to localize within a room, achieved localization accuracies of 0.3–0.8 m in previous works, see [20], [21], [24]–[26], [30]. Note that only the system in [24] performed a 5-DoF localization. Thereby, they achieved an elevation-error of 9.7° and an azimuth-error of 2.8°.

The remainder of this paper is organized in the following manner. Section II describes the system principle of the MLPS. Section III presents the mathematical model of the field sensors. Then, Section IV describes the calibration of the sensor model and localization with a least mean square (LMS) algorithm. Section V describes the hardware setup of the realized system. Section VI presents the measurement results with and without considering the sensor model. Finally, Section VII presents the conclusion.

II. SYSTEM PRINCIPLE

In Fig. 1, the MLPS principle is illustrated. The aim of the MLPS is to estimate the pose of a magnetic transmitter (TX), emitting a quasi-static magnetic field. In this paper, the magnetic field of the TX is described by a magnetic dipole
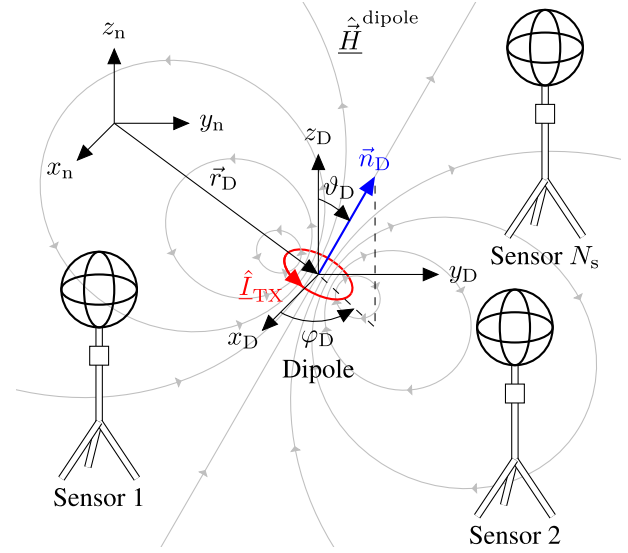

Fig. 1. Principle of localization of a magnetic dipole with a network comprising several field sensors, where x_D, y_D, and z_D denote the dipole's frame and x_n, y_n, and z_n denote the navigation frame.

in free space. The underscore marks a complex number, the hat an amplitude value, the arrow above the variable a vector, and matrices are written in bold letters. Assuming that the magnetic dipole is located at position $\vec{r}_D$ and oriented by a normal vector $\vec{n}_D = \vec{e}_x \sin \vartheta_D \cos \varphi_D + \vec{e}_y \sin \vartheta_D \sin \varphi_D + \vec{e}_z \cos \vartheta_D$, where ϑ_D is the elevation, φ_D denotes the azimuth angle, and $\vec{e}_x$, $\vec{e}_y$, and $\vec{e}_z$ are the basis vectors, the transmitted magnetic field at position $\vec{r}_P$ can be expressed as

$$\underline{\hat{\vec{H}}}^{\text{dipole}}(\vec{r}_P, \vec{x}_{\text{pose}}) = \frac{1}{4\pi r^3}\left[3\frac{\vec{r}}{r}\left(\frac{\vec{r}}{r}\cdot\underline{\hat{\vec{m}}}\right) - \underline{\hat{\vec{m}}}\right] \quad (1)$$

with $\vec{r} = \vec{r}_P - \vec{r}_D$, $r = |\vec{r}|$, the pose of the dipole $\vec{x}_{\text{pose}} = \left(\vec{r}_D^{\text{T}} \ \vartheta_D \ \varphi_D\right)^{\text{T}}$, $(\cdot)^{\text{T}}$ as transpose, the magnetic moment $\underline{\hat{\vec{m}}} = \underline{\hat{I}}_{\text{TX}} A_D \vec{n}_D$, $\underline{\hat{I}}_{\text{TX}}$ as current that flows through the dipole, and A_D the dipole area (see [32]). The magnetic field is measured at different positions in space with several 3-D-field sensors. The dipole's pose is estimated on the basis of the measurement data.

III. FIELD SENSOR IMPAIRMENT MODEL

Each field sensor comprises three coils. As mentioned, a variety of impairments occur. To be able to calibrate the effects of the field sensors, they are described mathematically in detail in this Section.

A. Magnetic Coupling

The left-hand side of Fig. 2 shows the magnetic TX and the right-hand side shows the three coils of a field sensor, where Φ denotes the magnetic flux. The losses of the coils are modeled with ohmic resistors. Capacitors are placed at the output of the circuit in order to create a resonance peak [33], [34]. With Faraday's law of induction, this yields the following equation
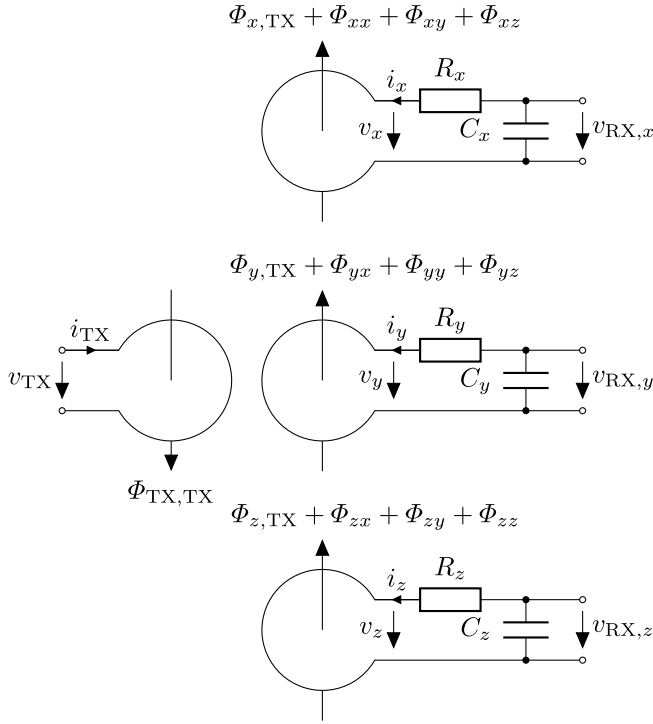
Fig. 2.   Network model and magnetic coupling of a field sensor.

in the time domain:

$$
\begin{pmatrix} v_{\text{TX}} \\ v_x \\ v_y \\ v_z \end{pmatrix} = \frac{\mathrm{d}}{\mathrm{d}t} \begin{pmatrix} \Psi_{\text{TX,TX}} \\ \Psi_{x,\text{TX}} + \Psi_{xx} + \Psi_{xy} + \Psi_{xz} \\ \Psi_{y,\text{TX}} + \Psi_{yx} + \Psi_{yy} + \Psi_{yz} \\ \Psi_{z,\text{TX}} + \Psi_{zx} + \Psi_{zy} + \Psi_{zz} \end{pmatrix}
$$

$$
= \frac{\mathrm{d}}{\mathrm{d}t} \begin{pmatrix} L_{\text{TX}} i_{\text{TX}} \\ M_{x,\text{TX}} i_{\text{TX}} + L_x i_x + M_{xy} i_y + M_{xz} i_z \\ M_{y,\text{TX}} i_{\text{TX}} + M_{yx} i_x + L_y i_y + M_{yz} i_z \\ M_{z,\text{TX}} i_{\text{TX}} + M_{zx} i_x + M_{zy} i_y + L_z i_z \end{pmatrix}
$$

$$
= \boldsymbol{L} \cdot \frac{\mathrm{d}}{\mathrm{d}t} \begin{pmatrix} i_{\text{TX}} \\ i_x \\ i_y \\ i_z \end{pmatrix} \tag{2}
$$

where the linked magnetic flux of circular coils with N windings can be stated as $\Psi \approx N\Phi$, L is the self-inductance, M is the mutual inductance, and backward coupling from the receiver (RX) side to the TX side is negligible. The inductance matrix [35] is expressed as

$$
\boldsymbol{L} = \begin{pmatrix} L_{\text{TX}} & \boldsymbol{0}_{1\times3} \\ \boldsymbol{L}_{\text{s,TX}} & \boldsymbol{L}_{\text{s,s}} \end{pmatrix} \tag{3}
$$

with

$$
\boldsymbol{L}_{\text{s,TX}} = \begin{pmatrix} M_{x,\text{TX}} \\ M_{y,\text{TX}} \\ M_{z,\text{TX}} \end{pmatrix}, \quad \boldsymbol{L}_{\text{s,s}} = \begin{pmatrix} L_x & M_{xy} & M_{xz} \\ M_{yx} & L_y & M_{yz} \\ M_{zx} & M_{zy} & L_z \end{pmatrix} \tag{4}
$$

where $\boldsymbol{L}_{\text{s,TX}}$ describes the coupling between the TX coil and the sensor coils and $\boldsymbol{L}_{\text{s,s}}$ the magnetic coupling within the field sensor. In the frequency domain follows with the angular frequency $\omega = 2\pi f$

$$
\begin{pmatrix} \hat{V}_{\text{TX}} \\ \hat{V}_x \\ \hat{V}_y \\ \hat{V}_z \end{pmatrix} = \mathrm{j}\omega \boldsymbol{L} \cdot \begin{pmatrix} \hat{I}_{\text{TX}} \\ \hat{I}_x \\ \hat{I}_y \\ \hat{I}_z \end{pmatrix}. \tag{5}
$$

The network's output in Fig. 2 can be described by two mesh equations, with $\xi \in \{x, y, z\}$, as

$$
\hat{I}_\xi = -\mathrm{j}\omega C_\xi \hat{V}_{\text{RX},\xi} \tag{6}
$$

$$
\hat{V}_\xi = -\hat{I}_\xi R_\xi + \hat{V}_{\text{RX},\xi} = (1 + \mathrm{j}\omega R_\xi C_\xi)\hat{V}_{\text{RX},\xi}. \tag{7}
$$

With (5), the voltage at the RX coils can be rewritten as

$$
\begin{pmatrix} \hat{V}_x \\ \hat{V}_y \\ \hat{V}_z \end{pmatrix} = \mathrm{j}\omega \underbrace{\boldsymbol{L}_{\text{s,TX}} \hat{I}_{\text{TX}}}_{=\hat{\underline{\psi}}_{\text{s,TX}}} + \mathrm{j}\omega \boldsymbol{L}_{\text{s,s}} \begin{pmatrix} \hat{I}_x \\ \hat{I}_y \\ \hat{I}_z \end{pmatrix}. \tag{8}
$$

Inserting (6) and (7) into (8) and reordering for the linked magnetic flux vector $\hat{\underline{\psi}}_{\text{s,TX}}$ yields

$$
\hat{\underline{\psi}}_{\text{s,TX}}
$$

$$
= \boldsymbol{L}_{\text{s,TX}} \hat{I}_{\text{TX}} = -\boldsymbol{L}_{\text{s,s}} \begin{pmatrix} \hat{I}_x \\ \hat{I}_y \\ \hat{I}_z \end{pmatrix} + \frac{1}{\mathrm{j}\omega} \begin{pmatrix} \hat{V}_x \\ \hat{V}_y \\ \hat{V}_z \end{pmatrix}
$$

$$
= \mathrm{j}\omega \boldsymbol{L}_{\text{s,s}} \begin{pmatrix} C_x & 0 & 0 \\ 0 & C_y & 0 \\ 0 & 0 & C_z \end{pmatrix} \hat{\underline{V}}_{\text{RX}}
$$

$$
+ \begin{pmatrix} \dfrac{1 + \mathrm{j}\omega R_x C_x}{\mathrm{j}\omega} & 0 & 0 \\ 0 & \dfrac{1 + \mathrm{j}\omega R_y C_y}{\mathrm{j}\omega} & 0 \\ 0 & 0 & \dfrac{1 + \mathrm{j}\omega R_z C_z}{\mathrm{j}\omega} \end{pmatrix} \hat{\underline{V}}_{\text{RX}}
$$

$$
= \boldsymbol{M}_{\text{coupling}} \cdot \hat{\underline{V}}_{\text{RX}} \tag{9}
$$

with the coupling matrix $\boldsymbol{M}_{\text{coupling}}$, which is shown at the bottom of this page. By assuming the field sensor to be free of

$$
\boldsymbol{M}_{\text{coupling}} = \begin{pmatrix} \dfrac{1 - \omega^2 L_x C_x}{\mathrm{j}\omega} + R_x C_x & \mathrm{j}\omega M_{xy} C_y & \mathrm{j}\omega M_{xz} C_z \\[2mm] \mathrm{j}\omega M_{yx} C_x & \dfrac{1 - \omega^2 L_y C_y}{\mathrm{j}\omega} + R_y C_y & \mathrm{j}\omega M_{yz} C_z \\[2mm] \mathrm{j}\omega M_{zx} C_x & \mathrm{j}\omega M_{zy} C_y & \dfrac{1 - \omega^2 L_z C_z}{\mathrm{j}\omega} + R_z C_z \end{pmatrix}
$$

coupling and resonance-matched circuits, the ideal relationship can be stated as

$$\hat{\underline{\vec{\Psi}}}_{s,TX} = \begin{pmatrix} R_x C_x & 0 & 0 \\ 0 & R_y C_y & 0 \\ 0 & 0 & R_z C_z \end{pmatrix} \hat{\underline{\vec{V}}}_{RX}$$

$$= \boldsymbol{M}_{\text{coupling,ideal}} \cdot \hat{\underline{\vec{V}}}_{RX}. \tag{10}$$

B. Misalignment of the Coils to the Body Frame

The magnetic flux $\hat{\underline{\Psi}}_{s,TX,\xi}$ flowing through a coil $\xi \in \{x, y, z\}$ can generally be evaluated by integrating the magnetic field strength flowing through a sensor at position $\vec{r}_s$ over the coil area as

$$\hat{\underline{\Psi}}_{s,TX,\xi} = \iint_{A_\xi} \mu_0 \hat{\underline{\vec{H}}}_n(\vec{r}_P) \cdot d\vec{A}_n \tag{11}$$

where $(\cdot)_n$ denotes navigation frame coordinates, μ_0 denotes vacuum permeability, and A_ξ denotes linked coil area. Now, expanding the magnetic field strength into its Taylor expansion around the center of symmetric coils, $\vec{r}_s$ reveals that every point symmetrical component of the magnetic field integrates over the coil area to zero. Hence, assuming the field to be almost described by the constant and linear Taylor component as

$$\hat{\underline{\vec{H}}}_n(\vec{r}_P) \approx \hat{\underline{\vec{H}}}_n(\vec{r}_s) + \left.\frac{\partial \hat{\underline{\vec{H}}}_n}{\partial \vec{r}_P}\right|_{\vec{r}_P=\vec{r}_s} (\vec{r}_P - \vec{r}_s) \tag{12}$$

allows to approximate the magnetic flux as

$$\begin{aligned}
\hat{\underline{\Psi}}_{s,TX,\xi} &\approx \iint_{A_\xi} \mu_0 \left(\hat{\underline{\vec{H}}}_n(\vec{r}_s) + \left.\frac{\partial \hat{\underline{\vec{H}}}_n}{\partial \vec{r}_P}\right|_{\vec{r}_P=\vec{r}_s} (\vec{r}_P - \vec{r}_s) \right) d\vec{A}_n \\
&= \iint_{A_\xi} \mu_0 \hat{\underline{\vec{H}}}_n(\vec{r}_s) \cdot d\vec{A}_n = A_\xi \vec{n}^{\text{T}}_{L_\xi,n} \cdot \mu_0 \hat{\underline{\vec{H}}}_n(\vec{r}_s) \\
&= A_\xi \vec{n}^{\text{T}}_{L_\xi,b} \underbrace{\boldsymbol{R}^{\text{T}}_{nb} \boldsymbol{R}_{nb}}_{=\boldsymbol{I}_3} \mu_0 \hat{\underline{\vec{H}}}_b(\vec{r}_s) = A_\xi \vec{n}^{\text{T}}_{L_\xi,b} \cdot \mu_0 \hat{\underline{\vec{H}}}_{s,b}
\end{aligned} \tag{13}$$

where $(\cdot)_b$ denotes body-frame coordinates, $\vec{n}_{L_\xi,b}$ denotes orientation vector of the ξth coil in body-frame coordinates, $\boldsymbol{R}_{nb}$ denotes the rotation matrix from the body frame to the navigation frame [36, p. 41], and $\hat{\underline{\vec{H}}}_{s,b} = \hat{\underline{\vec{H}}}_b(\vec{r}_s)$. Ideally, the orientation vectors of the coils can be expressed as

$$\vec{n}_{L_x,b,\text{ideal}} = \vec{e}_x = \vec{e}_r \left(\vartheta = \frac{\pi}{2}, \varphi = 0 \right) \tag{14}$$

$$\vec{n}_{L_y,b,\text{ideal}} = \vec{e}_y = \vec{e}_r \left(\vartheta = \frac{\pi}{2}, \varphi = \frac{\pi}{2} \right) \tag{15}$$

$$\vec{n}_{L_z,b,\text{ideal}} = \vec{e}_z = \vec{e}_r (\vartheta = 0, \varphi = 0) \tag{16}$$

with $\vec{e}_r(\vartheta, \varphi) = \vec{e}_x \sin\vartheta \cos\varphi + \vec{e}_y \sin\vartheta \sin\varphi + \vec{e}_z \cos\vartheta$ and r, ϑ, and φ as spherical coordinates. Unfortunately, misalignment of the coil's orientation vectors with respect to the body-frame coordinate system of the field sensor occurs due to inaccurate coil assembling and by the slope of the

coil's winding. Then, (13) can be written for every coil as

$$\begin{aligned}
\hat{\underline{\vec{\Psi}}}_{s,TX} &= \begin{pmatrix} A_x \vec{n}^{\text{T}}_{L_x,b} \cdot \mu_0 \hat{\underline{\vec{H}}}_{s,b} \\ A_y \vec{n}^{\text{T}}_{L_y,b} \cdot \mu_0 \hat{\underline{\vec{H}}}_{s,b} \\ A_z \vec{n}^{\text{T}}_{L_z,b} \cdot \mu_0 \hat{\underline{\vec{H}}}_{s,b} \end{pmatrix} \\
&= \begin{pmatrix} A_x & 0 & 0 \\ 0 & A_y & 0 \\ 0 & 0 & A_z \end{pmatrix} \cdot \boldsymbol{M}_{\text{misalignment}} \cdot \mu_0 \hat{\underline{\vec{H}}}_{s,b}
\end{aligned} \tag{17}$$

with the misalignment matrix

$$\boldsymbol{M}_{\text{misalignment}} = \begin{pmatrix} \vec{n}^{\text{T}}_{L_x,b} \\ \vec{n}^{\text{T}}_{L_y,b} \\ \vec{n}^{\text{T}}_{L_z,b} \end{pmatrix}. \tag{18}$$

The ideal misalignment matrix is the identity matrix

$$\boldsymbol{M}_{\text{misalignment,ideal}} = \begin{pmatrix} \vec{n}^{\text{T}}_{L_x,b,\text{ideal}} \\ \vec{n}^{\text{T}}_{L_y,b,\text{ideal}} \\ \vec{n}^{\text{T}}_{L_z,b,\text{ideal}} \end{pmatrix} = \boldsymbol{I}_3. \tag{19}$$

Then, the misalignment between the coil's orientation vector and the body-frame of the sensor can be described with error angles in spherical coordinates, thereby yielding the following true coil orientation vector

$$\vec{n}_{L_x,b} = \vec{e}_r \left(\vartheta = \frac{\pi}{2} + \vartheta_{e,x}, \varphi = \varphi_{e,x} \right) \tag{20}$$

$$\vec{n}_{L_y,b} = \vec{e}_r \left(\vartheta = \frac{\pi}{2} + \vartheta_{e,y}, \varphi = \frac{\pi}{2} + \varphi_{e,y} \right) \tag{21}$$

$$\vec{n}_{L_z,b} = \vec{e}_r (\vartheta = \vartheta_{e,z}, \varphi = \varphi_{e,z}). \tag{22}$$

The misalignment matrix can now be stated as

$$\begin{aligned}
& \boldsymbol{M}_{\text{misalignment}} \\
&= \begin{pmatrix} \vec{n}^{\text{T}}_{L_x,b} \\ \vec{n}^{\text{T}}_{L_y,b} \\ \vec{n}^{\text{T}}_{L_z,b} \end{pmatrix} \\
&= \begin{pmatrix} \cos\vartheta_{e,x}\cos\varphi_{e,x} & \cos\vartheta_{e,x}\sin\varphi_{e,x} & -\sin\vartheta_{e,x} \\ -\cos\vartheta_{e,y}\sin\varphi_{e,y} & \cos\vartheta_{e,y}\cos\varphi_{e,y} & -\sin\vartheta_{e,y} \\ \sin\vartheta_{e,z}\cos\varphi_{e,z} & \sin\vartheta_{e,z}\sin\varphi_{e,z} & \cos\vartheta_{e,z} \end{pmatrix}.
\end{aligned} \tag{23}$$

C. Rotation With Respect to the Navigation Frame

The rotation of the field sensor with respect to the navigation frame can be described by the rotation of the magnetic field strength vector in navigation coordinates to the sensor's body frame with a direction cosine matrix

$$\hat{\underline{\vec{H}}}_{s,b} = \boldsymbol{R}_{bn} \cdot \hat{\underline{\vec{H}}}_{s,n} \tag{24}$$

where $\boldsymbol{R}_{bn}$ denotes the rotation from the navigation frame to the body frame [36, p. 41].

D. Effects of the Circuit and Signal Processing

As shown in (1), the magnetic field strength is proportional to $1/r^3$. Therefore, the RX circuit needs to sustain a large signal dynamic. For this purpose, several parallel signal processing chains supporting different signal levels
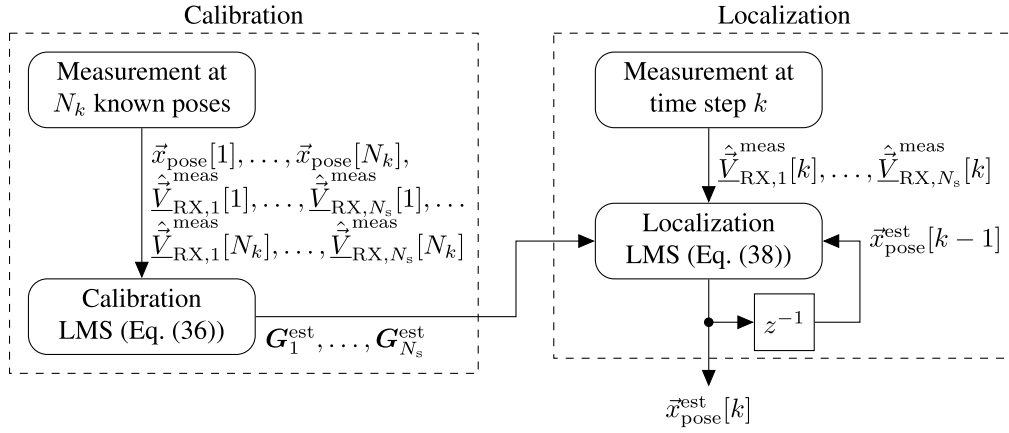
Fig. 3. Algorithm flowchart showing the calibration on the left-hand side and the localization on the right-hand side.

are required. The signal after the analog and digital signal processing chain ν is given as

$$\hat{\underline{\vec{s}}}_\nu = \begin{pmatrix} \underline{a}_{\nu,x} & 0 & 0 \\ 0 & \underline{a}_{\nu,y} & 0 \\ 0 & 0 & \underline{a}_{\nu,z} \end{pmatrix} \hat{\underline{\vec{V}}}_{\text{RX}} = \boldsymbol{A}_\nu \cdot \hat{\underline{\vec{V}}}_{\text{RX}} \qquad (25)$$

with the amplification matrix $\boldsymbol{A}_\nu$ and the amplification factors $\underline{a}_{\nu,\xi}$ for each channel with $\xi \in \{x, y, z\}$, including the influences of voltage dividers, amplifiers, analog-to-digital converters (ADCs), and other linear operations in the signal chain that alter the signal's phase and amplitude. The measured voltage $\hat{\underline{\vec{V}}}_{\text{RX}}$ is calculated manually by a measured amplification matrix per signal chain from the signal $\hat{\underline{\vec{s}}}_\nu$ and has no impact on the subsequent calibration scheme.

E. Complete Field Sensor Model

The overall transfer model of the magnetic field strength flowing through the sensor coils and the RX voltage follows from (9) and (17) as

$$\hat{\underline{\vec{V}}}_{\text{RX}} = \boldsymbol{M} \cdot \hat{\underline{\vec{H}}}_{\text{s,b}} \qquad (26)$$

with

$$\boldsymbol{M} = \mu_0 \cdot \boldsymbol{M}_{\text{coupling}}^{-1} \begin{pmatrix} A_x & 0 & 0 \\ 0 & A_y & 0 \\ 0 & 0 & A_z \end{pmatrix} \boldsymbol{M}_{\text{misalignment}} \qquad (27)$$

as the sensor's model matrix. Hence, all field sensor effects can be described by a single matrix relation. The ideal model matrix is given with (10) and (19) as

$$\boldsymbol{M}_{\text{ideal}} = \begin{pmatrix} \dfrac{\mu_0 \cdot A_x}{R_x C_x} & 0 & 0 \\ 0 & \dfrac{\mu_0 \cdot A_y}{R_y C_y} & 0 \\ 0 & 0 & \dfrac{\mu_0 \cdot A_z}{R_z C_z} \end{pmatrix}. \qquad (28)$$

Adding the rotation of the field sensor results in

$$\hat{\underline{\vec{V}}}_{\text{RX}} = \boldsymbol{M} \cdot \boldsymbol{R}_{\text{bn}} \cdot \hat{\underline{\vec{H}}}_{\text{s,n}}. \qquad (29)$$

F. Sampling Effects

As the implementation of distributing a common sampling clock for synchronization to each field sensor and magnetic TX comes with disproportional hardware effort, only the signals at the three coils of every field sensor are sampled coherently. Hence, every sensor has a common random signal phase $\alpha[k]$ at each coil at measurement point k resulting in

$$\hat{\underline{\vec{V}}}_{\text{RX}}[k] = \boldsymbol{M} \cdot \boldsymbol{R}_{\text{bn}} \cdot \hat{\underline{\vec{H}}}_{\text{s,n}}[k] \cdot \text{e}^{\text{j}\alpha[k]}. \qquad (30)$$

IV. CALIBRATION AND LOCALIZATION ALGORITHM

In this section, a novel calibration and corresponding localization scheme are developed, which are designed to deal with the considered hardware impairments. For this purpose, a noise model and its impact on the statistical optimal localization are examined. Furthermore, a corresponding novel field sensor calibration is developed. This results in two LMS algorithms directly comparing magnetic field strengths that can be solved with gradient-based algorithms, which are generally combining high precision with low computational effort. In addition, an analytical solution is derived in order to handle the effects originated from unsynchronized sampling. Fig. 3 shows the flowchart of the subsequently proposed algorithm. It consists of the foregoing calibration on the left-hand side and the recursive localization on the right-hand side.

A. Noise Model

In this paper, the magnetic field is assumed to be disturbed by additive complex zero mean white Gaussian noise $\underline{\vec{w}}[k] \sim \mathcal{CN}_3(\vec{0}, \sigma^2 \boldsymbol{I})$, which is well known from communications, see [37]. Thereby, the noise arises from the superposition of different error sources like electric devices or coupling of the magnetic field with the environment. Furthermore, additive white Gaussian noise represents a worst case scenario, see [37]. As $\underline{\vec{w}}[k]$ is disturbing the magnetic field, the measured voltage at field sensor η can be stated with (30) as

$$\hat{\underline{\vec{V}}}_{\text{RX},\eta}^{\text{meas}}[k] = \boldsymbol{G}_\eta^{-1}\left(\hat{\underline{\vec{H}}}_{s_\eta,\text{n}}^{\text{dipole}}[k] + \underline{\vec{w}}[k]\right)\text{e}^{\text{j}\alpha_\eta[k]} \qquad (31)$$

with the dipole field $\hat{\underline{\vec{H}}}_{s_\eta,n}^{dipole} = \hat{\underline{\vec{H}}}_n^{dipole}(\vec{r}_{s_\eta}, \vec{x}_{pose})$, as in (1), $G_\eta^{-1} = M_\eta R_{bn,\eta}$, and hence, the measured magnetic field strength as

$$
\begin{aligned}
\hat{\underline{\vec{H}}}_{s_\eta,n}^{meas}[k] &= G_\eta \hat{\underline{\vec{V}}}_{RX,\eta}^{meas}[k] \\
&= \left(\hat{\underline{\vec{H}}}_{s_\eta,n}^{dipole}[k] + \underline{\vec{w}}[k] \right) \cdot e^{j\alpha_\eta[k]} \\
&= \hat{\underline{\vec{H}}}_{s_\eta,n}^{dipole}[k] \cdot e^{j\alpha_\eta[k]} + \underline{\vec{w}}'[k]
\end{aligned}
\tag{32}
$$

with $\underline{\vec{w}}'[k] = \underline{\vec{w}}[k] \cdot e^{j\alpha_\eta[k]}$. Thereby, $\underline{\vec{w}}'[k] \sim \mathcal{CN}_3(\vec{0}, \sigma^2 I)$ holds as Gaussian noise is phase-shift invariant. Note that the assumption about the noise appearance is essential, as the measured noise at $\hat{\underline{\vec{V}}}_{RX,\eta}^{meas}[k]$ becomes correlated in (31) due to the matrix multiplication with G_η^{-1}.

B. Maximum Likelihood Estimation

In order to calibrate the model and accordingly localize the magnetic TX, the likelihood function [38, pp. 542–547]

$$
\begin{aligned}
P = \prod_{\eta=1}^{N_s} \prod_{k=1}^{N_k} \prod_{\xi} \frac{1}{\pi\sigma^2} \\
\cdot \exp\left(-\frac{\left| \hat{H}_{s_\eta,n,\xi}^{meas}[k] - \hat{H}_{s_\eta,n,\xi}^{dipole}[k]e^{j\alpha_\eta[k]} \right|^2}{\sigma^2} \right)
\end{aligned}
\tag{33}
$$

has to be maximized, where N_s and N_k denote the number of field sensors and measurement points, respectively, and $\xi \in \{x, y, z\}$ and $|\cdot|$ denote absolute value. As $\ln(\cdot)$ is a monotonic function, the maximization of (33) is equivalent to the maximization of its log-likelihood function

$$
\begin{aligned}
\ln(P) = {}& -3N_s N_k \ln\left(\pi\sigma^2\right) - \frac{1}{\sigma^2} \\
&\cdot \sum_{\eta=1}^{N_s} \sum_{k=1}^{N_k} \sum_{\xi} \left| \hat{H}_{s_\eta,n,\xi}^{meas}[k] - \hat{H}_{s_\eta,n,\xi}^{dipole}[k]e^{j\alpha_\eta[k]} \right|^2.
\end{aligned}
\tag{34}
$$

Thus, both the calibration and the localization is performed by solving

$$
\begin{aligned}
&\max_{\vec{x}} \left(-\sum_{\eta=1}^{N_s} \sum_{k=1}^{N_k} \sum_{\xi} \left| \hat{H}_{s_\eta,n,\xi}^{meas}[k] - \hat{H}_{s_\eta,n,\xi}^{dipole}[k]e^{j\alpha_\eta[k]} \right|^2 \right) \\
&= \min_{\vec{x}} \sum_{\eta=1}^{N_s} \sum_{k=1}^{N_k} \left\| \hat{\underline{\vec{H}}}_{s_\eta,n}^{meas}[k] - \hat{\underline{\vec{H}}}_{s_\eta,n}^{dipole}[k]e^{j\alpha_\eta[k]} \right\|_2^2 \\
&= \min_{\vec{x}} \sum_{\eta=1}^{N_s} \sum_{k=1}^{N_k} \left\| G_\eta \hat{\underline{\vec{V}}}_{RX,\eta}^{meas}[k] - \hat{\underline{\vec{H}}}_{s_\eta,n}^{dipole}[k]e^{j\alpha_\eta[k]} \right\|_2^2
\end{aligned}
\tag{35}
$$

where $\|\cdot\|_2$ denotes the Euclidean norm and $\vec{x}$ denotes the vector containing the optimization variables.

C. Sensor Model Estimation

The sensor model estimation of sensor η is executed by recording N_k measurement points with different known TX poses. Here, random TX poses to support the assumption of

uncorrelated Gaussian noise, as in (31). The field sensors can be calibrated independently of each other, as in (35), the corresponding errors are summed up. Hence, for estimating G_η

$$
\begin{aligned}
&\min_{G_\eta, \alpha_\eta[1], \dots, \alpha_\eta[N_k]} \sum_{k=1}^{N_k} \left\| G_\eta \hat{\underline{\vec{V}}}_{RX,\eta}^{meas}[k] - \hat{\underline{\vec{H}}}_{s_\eta,n}^{dipole}[k]e^{j\alpha_\eta[k]} \right\|_2^2 \\
&= \min_{G_\eta} \sum_{k=1}^{N_k} \min_{\alpha_\eta[k]} \left\| G_\eta \hat{\underline{\vec{V}}}_{RX,\eta}^{meas}[k] - \hat{\underline{\vec{H}}}_{s_\eta,n}^{dipole}[k]e^{j\alpha_\eta[k]} \right\|_2^2 \\
&\overset{(a)}{=} \min_{G_\eta} \sum_{k=1}^{N_k} \left\| G_\eta \hat{\underline{\vec{V}}}_{RX,\eta}^{meas}[k] - \hat{\underline{\vec{H}}}_{s_\eta,n}^{dipole}[k]e^{j\alpha'_\eta[k]} \right\|_2^2
\end{aligned}
\tag{36}
$$

needs to be solved, where (42) is used at (a) (see Appendix), and $\alpha'_\eta[k] = -\arg\{\hat{\underline{\vec{H}}}_{s_\eta,n}^{meas,H}[k]\hat{\underline{\vec{H}}}_{s_\eta,n}^{dipole}[k]\}$. Inserting $G_\eta^{est} = G_\eta e^{j\alpha_{e,\eta}}$ and $\alpha_\eta^{est}[k] = \alpha_\eta[k] + \alpha_{e,\eta}$, with the unknown phase $\alpha_{e,\eta}$, into the kth summand of (36) as

$$
\begin{aligned}
&\left\| G_\eta^{est} \hat{\underline{\vec{V}}}_{RX,\eta}^{meas}[k] - \hat{\underline{\vec{H}}}_{s_\eta,n}^{dipole}[k]e^{j\alpha_\eta^{est}[k]} \right\|_2^2 \\
&= \left\| e^{j\alpha_{e,\eta}} \left(G_\eta \hat{\underline{\vec{V}}}_{RX,\eta}^{meas}[k] - \hat{\underline{\vec{H}}}_{s_\eta,n}^{dipole}[k]e^{j\alpha_\eta[k]} \right) \right\|_2^2 \\
&= \left\| G_\eta \hat{\underline{\vec{V}}}_{RX,\eta}^{meas}[k] - \hat{\underline{\vec{H}}}_{s_\eta,n}^{dipole}[k]e^{j\alpha_\eta[k]} \right\|_2^2
\end{aligned}
\tag{37}
$$

shows that the overall calibration metric for G_η is insensitive to a phase shift. Hence, in order to assure the stable convergence to the optimal solution for G_η, it is assumed that $\text{Im}\{G_\eta[1,1]\} = 0$. Generally, except for the unknown phases $\alpha_\eta[1], \dots, \alpha_\eta[N_k]$, the optimization problem in (36) is linear least square. As the phases are evaluated analytically, see Appendix, the remaining search is well-suited for a gradient-based search beginning from $G_{\eta,start} = M_{ideal}^{-1}$. Note that due to the phase ambiguity $-G_\eta$ is an equivalently accurate solution to G_η. However, as $G_{\eta,start}[1,1] > 0$ holds, G_η will converge toward its positive solution.

D. Estimation of the Pose of the Magnetic Dipole

Similar to the calibration of the individual field sensors, the TX poses can be estimated independent of each other by solving (35) for every measurement point k as

$$
\begin{aligned}
&\min_{\vec{x}_{pose}[k], \alpha_1[k], \dots, \alpha_{N_s}[k]} \sum_{\eta=1}^{N_s} \left\| \hat{\underline{\vec{H}}}_{s_\eta,n}^{meas}[k] - \hat{\underline{\vec{H}}}_{s_\eta,n}^{dipole}[k]e^{j\alpha_\eta[k]} \right\|_2^2 \\
&= \min_{\vec{x}_{pose}[k]} \sum_{\eta=1}^{N_s} \min_{\alpha_\eta[k]} \left\| \hat{\underline{\vec{H}}}_{s_\eta,n}^{meas}[k] - \hat{\underline{\vec{H}}}_{s_\eta,n}^{dipole}[k]e^{j\alpha_\eta[k]} \right\|_2^2 \\
&\overset{(a)}{=} \min_{\vec{x}_{pose}[k]} \sum_{\eta=1}^{N_s} \left\| \hat{\underline{\vec{H}}}_{s_\eta,n}^{meas}[k] - \hat{\underline{\vec{H}}}_{s_\eta,n}^{dipole}[k]e^{j\alpha'_\eta[k]} \right\|_2^2
\end{aligned}
\tag{38}
$$

where at (a) again (42) was used. For this purpose, a gradient-based search for pose $\vec{x}_{pose}[k]$ beginning from the previous pose $\vec{x}_{pose}[k-1]$ is well suited.

V. SYSTEM SETUP

Fig. 4 illustrates the block diagram of the TX and Fig. 5(a) illustrates its implementation. The system frequency is selected
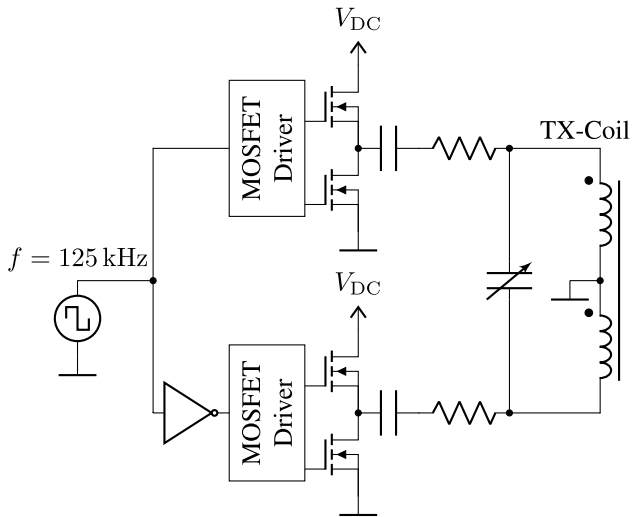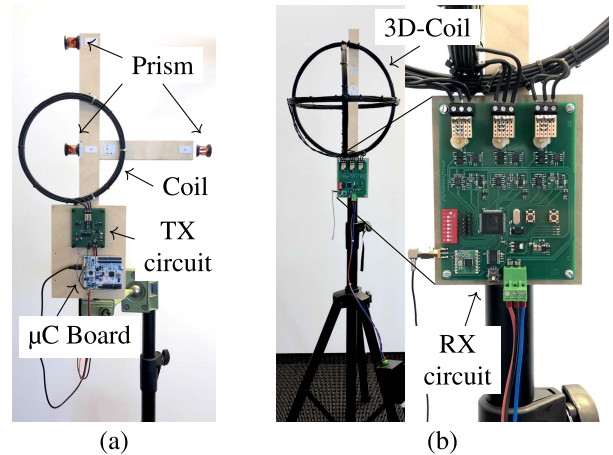
Fig. 4. Concept of the implemented TX.

Fig. 5. Implementation of (a) TX including driver circuit, microcontroller board, TX coil, and prisms for reference orientation and (b) field sensor consisting of 3-D-coil, RX circuit, microcontroller, and radio module.

to 125 kHz, because it turned out to be a good compromise in the tradeoff between a sufficiently strong receive signal and low coupling with the environment. A microcontroller board is used as a signal generator that generates a rectangular waveform at the system frequency. The noninverted rectangular signal and its inverted version are connected to MOSFET-driver circuits that control two n-channel MOSFETs in a half-bridge circuit. The MOSFETs connect the output to $V_{DC} = 48$ V and ground (GND) in an alternating manner. The upper signal path interacts with the lower signal path in a push–pull configuration. With the emerging differential output signal, the coil circuit is conducted by a rectangular signal with a peak-to-peak value of 2 V_{DC}. A tunable capacitor is connected in parallel to the TX coil to tune the resonance frequency of the parallel resonance circuit. Due to the filter behavior of the resonance circuit, the emerging coil current becomes sinusoidal at the system frequency with a measured amplitude of $\hat{I}_{TX} \approx 422$ mA. V_{DC} is generated by a boost-converter circuit, supplied by a 5 V power bank. The power consumption of the TX is 1.25 W.

The block diagram of a 3-D-field sensor is illustrated in Fig. 6 and its implementation is illustrated in Fig. 5(b). The resonance circuits with the three sensor coils are matched to the system frequency by tunable capacitors. During the tuning process, only one coil circuit is connected to its capacitors in order to avoid distorted measurements due to coil coupling. To ensure a high-quality factor in the resonance circuits, a buffer with a high impedance input follows. As the magnetic field strength is proportional to $1/r^3$, as in (1), the RX needs to manage a high dynamic range. For this purpose, the signal path is divided into an amplifier path (Amp) with an amplification factor of 10 and voltage divider path (AT) with an amplification factor of 0.1. A microcontroller of the type STM32F303VE is used for signal processing and communication. The signal paths are selected by a multiplexer (MUX) within the microcontroller. Subsequently, the signal is sampled by an ADC with a 12-Bit resolution and a sample rate of 480 kS/s, which satisfies the Nyquist–Shannon sampling theorem. The sampled signal of length 1024 is multiplied with

a flattop window and transformed to frequency domain using the discrete Fourier transform (DFT) algorithm. For noisy environments, a longer DFT, i.e., measuring time, might be used. Then, the amplitude of the spectral line, which represents the measured field strength, is stored as measurement at time k. If the peak value exceeds a threshold value, the MUX selects the voltage divider signal path. All sensors are connected to a sensor network via 433 MHz radio modules and with a unique address, which is configured by coding switches. The sensor network can be controlled by a host computer.

The TX and RX coils were dimensioned using the methods proposed in [34]. The circular coils have 20 windings of polyvinyl chloride-isolated wire with a cross section of 1.5 mm^2. The TX coils have a radius of 10 cm, and a simulated inductance and resistance of 155 μH and 1.02 Ω, respectively. The RX coils have a radius of 15 cm, and a simulated inductance and resistance of 258 μH and 1.48 Ω, respectively.

Fig. 7 illustrates the measurement setup for evaluating the proposed algorithms. The field sensor network comprises eight field sensors. In order to maximize the sensitivity of the measured magnetic fields to TX position changes, the field sensors were placed at the edges of the room. Furthermore, the field sensors need to cover the complete room in all three dimensions. Field sensors #1, #5, #8, and #4 can be seen in Fig. 7 from left to right. A tachymeter providing 3 mm accuracy measures the reference trajectory and orientation of the TX. The reference orientation is calculated by capturing the coordinates of three prisms [see Fig. 5(a)]. The office environment, in which the measurement was conducted, has a size of 7 m × 5 m × 3 m.

VI. MEASUREMENT RESULTS

At first, an approximation of the SNR of the measurement will be given. In this measurement, a field sensor was located at position $\vec{0}$ and the magnetic TX at $\vec{r}_D = (4\text{m} \ 0 \ 0)^T$ and y-orientated. Fig. 8 shows the DFT of the field sensor's y-channel. By performing two measurements with and without the TX, the SNR can be approximated to be about 60 dB at 4 m distance. Note that the TX localization
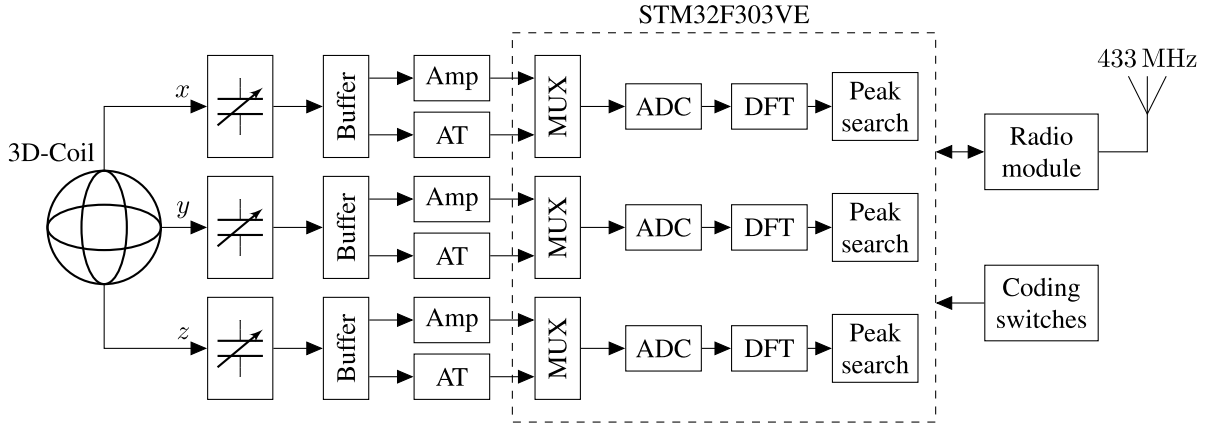
Fig. 6. Block diagram of the implemented field sensor. The signal path, either attenuator (AT) or amplifier (Amp), are selected with the MUX depending on the received signal amplitude. This way it was possible to cover the very high dynamic range with a 12-Bit ADC.
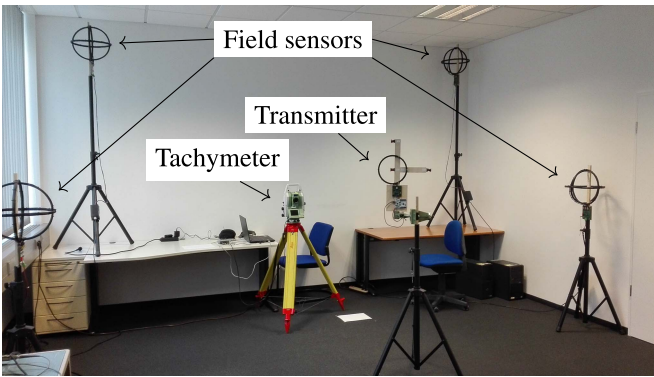

Fig. 7. Measurement setup for calibration and localization showing several field sensors, the TX, and a tachymeter for measurement of reference points and orientation.
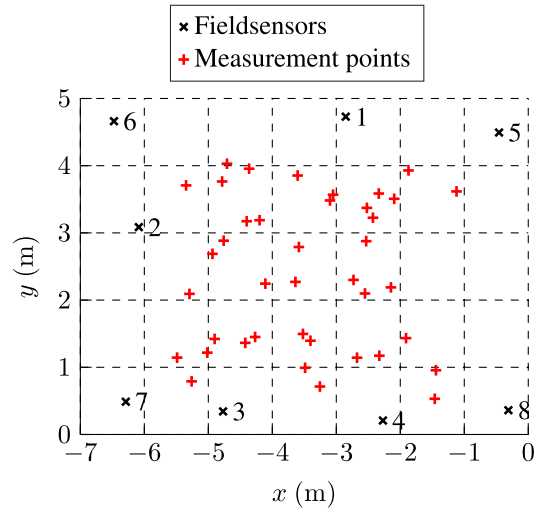

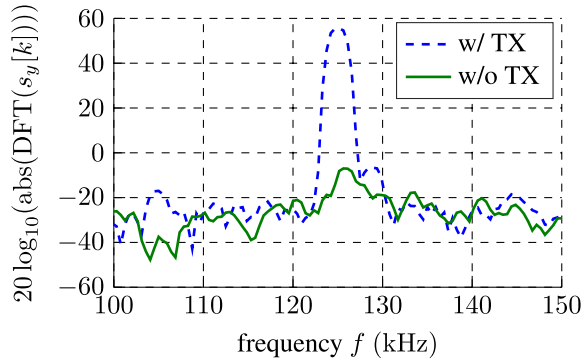Fig. 8. DFT of a coil's receive signal with and without TX. The y-oriented TX was located in 4 m x-distance to the y-oriented RX coil.

Fig. 9. Field sensor positions and measurement points used for calibration.

localization accuracy, the root-mean-square error (RMSE)

$$\text{RMSE}_{\text{pos}} = \sqrt{\frac{1}{N_k} \sum_{k=1}^{N_k} \left\| \vec{r}_{\text{D}}^{\text{est}}[k] - \vec{r}_{\text{D}}^{\text{ref}}[k] \right\|_2^2} \qquad (39)$$

is used. In order to analyze the orientation accuracy, the angle between the reference and estimated normal vector is calculated by the scalar product

$$\epsilon[k] = \arccos\left(\vec{n}_{\text{D}}^{\text{est}}[k] \cdot \vec{n}_{\text{D}}^{\text{ref}}[k]\right) \qquad (40)$$

and then yields the RMSE value of the error angle $\epsilon[k]$ as

$$\text{RMSE}_{\text{angle}} = \sqrt{\frac{1}{N_k} \sum_{k=1}^{N_k} \left\| \epsilon[k] \right\|_2^2}. \qquad (41)$$

As the field sensors are not synchronized with the magnetic TX, the direction of $\hat{\underline{I}}_{\text{TX}}$ in (1) is undetermined, which yields an uncertain sign of the orientation vector. This is fixed by knowledge of the start orientation and a fast sample rate of the localization system, where the orientation vector is located in the same half sphere as the orientation vector of the previous measurement point.

is performed via signal amplitude comparison, and hence, the SNR strongly depends on the TX location and orientation.

In Fig. 9, the positions of the field sensors and the measurement points for calibration are depicted. For this purpose, 40 measurements were conducted. In order to support the assumption of independent Gaussian noise in (31), the calibration was performed at random poses distributed over the entire measurement area. For evaluation of the localization accuracy, a trajectory with 100 measurement points was recorded. The reference trajectory was measured by the tachymeter and is shown as a red solid curve in Fig. 10. To specify the
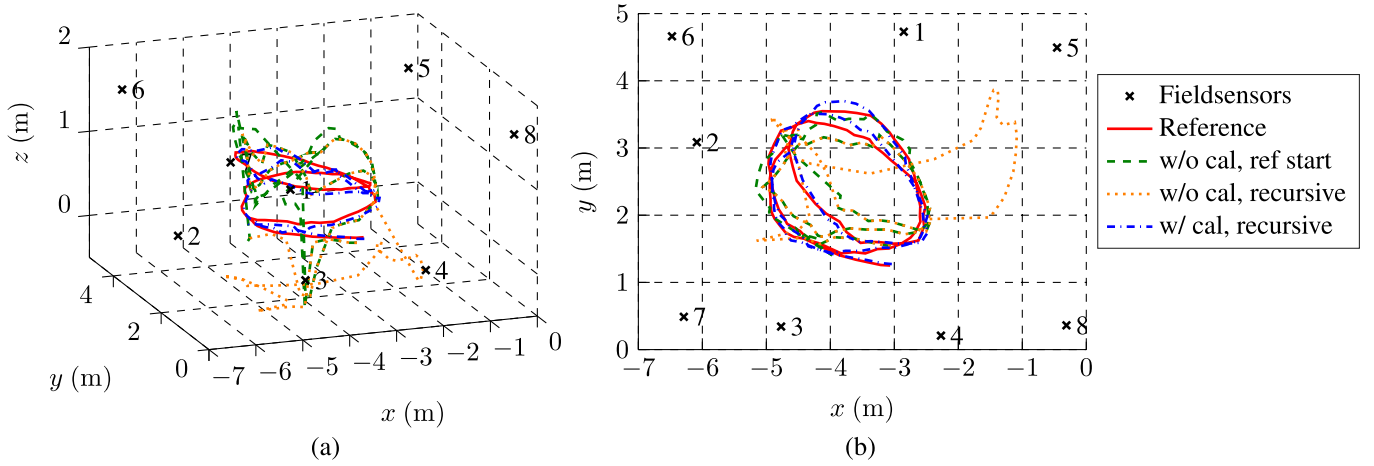
Fig. 10. (a) Side view and (b) top view of field sensor positions, reference trajectory, estimated trajectory by locating the TX searching from corresponding reference pose with uncalibrated field sensors, estimated trajectory by recursively locating the TX searching from its preceding pose with uncalibrated field sensors, and estimated trajectory by recursively locating the TX by searching from its preceding pose with calibrated field sensors.
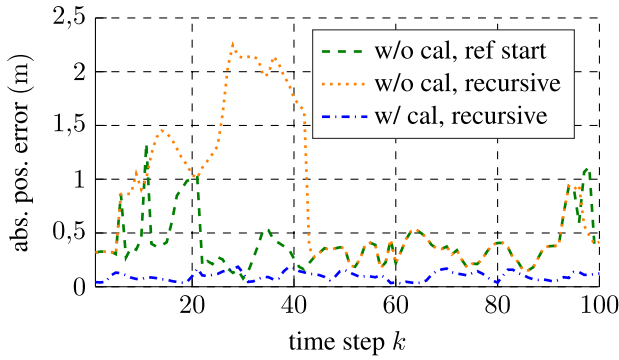

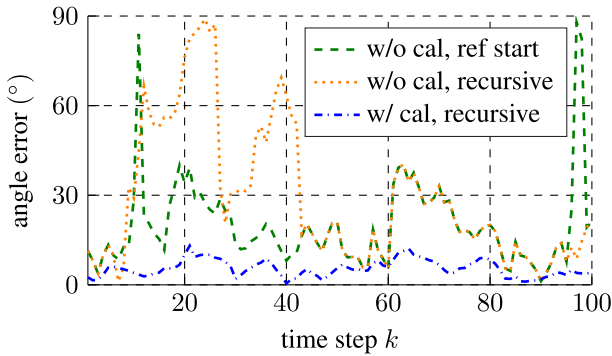Fig. 11. Position error of the estimated trajectories for each measurement point k shown in Fig. 10.

Fig. 12. Angle error from (40) of the estimated trajectories for each measurement point k shown in Fig. 10.

Fig. 13. Position and angle error histograms of pose estimation with calibrated field sensors.

In order to allow a fair comparison of calibrated and uncalibrated field sensors, the entries of the main diagonal of $\boldsymbol{M}_{\mathrm{ideal}}$ were individually measured by performing a reference measurement with a coil at a 2 m distance. In the uncalibrated case, coupling and misalignment of the sensor coils are neglected and thus $\boldsymbol{G}_{\mathrm{uncal}}^{-1} = \boldsymbol{M}_{\mathrm{ideal}}\boldsymbol{R}_{\mathrm{bn}}$, with known rotation matrices $\boldsymbol{R}_{\mathrm{bn}}$, is used for localization. The TX is located by recursively estimating the TX position $\vec{x}_{\mathrm{pose}}[k]$ with the pre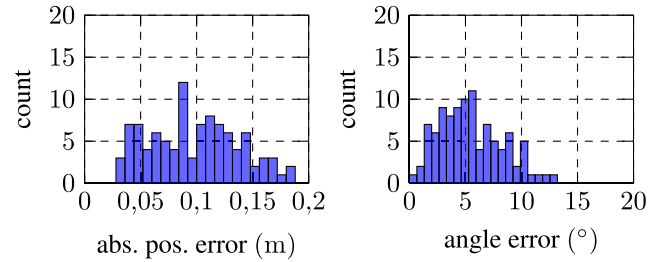vious point $\vec{x}_{\mathrm{pose}}[k-1]$ used as the initial value for the search algorithm. Generally, the algorithm could fail to converge toward the next global minimum due to erroneous measurements. In practice, this should be resolved by exploiting movement statistics, which might be done by a Kalman filter [27].

The overall localization results are shown in Fig. 10. The position and angle errors are shown in Figs. 11 and 12, respectively. The results for the uncalibrated and the calibrated field sensors are depicted by the orange dotted and the blue dashed–dotted line, respectively. The performance with uncalibrated field sensors is drastically degraded by the ambiguity of the least square solution of (38). The poses $\vec{x}_{\mathrm{pose}}[k]$ were also searched using the reference trajectory as initial values. The calibrated system maintains its accuracy, while the uncalibrated system improves its performance, as shown in the green dashed line, with a localization and orientation accuracy of 46.8 cm and 24.8°. Calibration of the system drastically improves the performance to 10.6 cm and 6.1°, respectively. Fig. 13 shows the histograms of the position and angle errors for calibrated field sensors. The localization error of the uncalibrated system agrees with comparable previous works, which is in the range of 0.3 to 0.8 m, see [20], [21], [24]–[26], [30]. In [24], an MLPS utilizing one-axis field sensors is shown, which achieves an elevation error of 9.7° and an azimuth error of 2.8°. The result approximately matches the orientation accuracy localized with the calibrated field sensors.

VII. Conclusion

In this paper, a variety of 3-D-field sensor impairments have been analyzed. Then, corresponding calibration and localization algorithms were proposed. It was shown, that the position- and orientation-RMSE could be drastically improved by calibration, which was demonstrated in a common office room. Considering the improved accuracy, MLPS becomes a promising candidate for high-accuracy indoor localization compared to other localization technologies like UWB.

Nevertheless, some subjects for further investigation emerged during measurements. At first, the influence of system parameters as TX signal strength and the number and positions of the field sensors should be examined. Furthermore, the measurements suggest that the main remaining challenge is the composition of the GND, which might be conductive, for example, ferroconcrete. Hence, incorporating the room into the calibration could be beneficial. Then, the positioning accuracy might be improved using statistical filters, e.g., a Kalman filter. Thereby, merging MLPS and other systems like INS will further increase localization performance and resolve the ambiguity challenge of MLPS.

Appendix

In this Appendix, it is shown that the optimization problem in (36) and (38) can be solved as

$$\underset{\alpha_\eta[k]}{\arg\min} \left\| \hat{\underline{H}}_{s_\eta,n}^{\text{meas}}[k] - \hat{\underline{H}}_{s_\eta,n}^{\text{dipole}}[k]e^{j\alpha_\eta[k]} \right\|_2^2$$
$$= -\arg\left\{ \hat{\underline{H}}_{s_\eta,n}^{\text{meas,H}}[k]\hat{\underline{H}}_{s_\eta,n}^{\text{dipole}}[k] \right\}. \quad (42)$$

For this purpose, the Hilbert projection theorem [38, pp. 116–118] is used, stating that for the optimal phase $\alpha_\eta[k]$ the remaining error $\hat{\underline{H}}_{s_\eta,n}^{\text{meas}}[k] - \hat{\underline{H}}_{s_\eta,n}^{\text{dipole}}[k] \cdot e^{j\alpha_\eta[k]}$ is orthogonal to $\hat{\underline{H}}_{s_\eta,n}^{\text{dipole}}[k] \cdot e^{j\alpha_\eta[k]}$. Thus

$$\left\langle \hat{\underline{H}}_{s_\eta,n}^{\text{meas}}[k] - \hat{\underline{H}}_{s_\eta,n}^{\text{dipole}}[k] \cdot e^{j\alpha_\eta[k]}, \hat{\underline{H}}_{s_\eta,n}^{\text{dipole}}[k] \cdot e^{j\alpha_\eta[k]} \right\rangle$$
$$= \left(\hat{\underline{H}}_{s_\eta,n}^{\text{meas}}[k] - \hat{\underline{H}}_{s_\eta,n}^{\text{dipole}}[k] \cdot e^{j\alpha_\eta[k]} \right)^{\text{H}} \hat{\underline{H}}_{s_\eta,n}^{\text{dipole}}[k] \cdot e^{j\alpha_\eta[k]}$$
$$= \hat{\underline{H}}_{s_\eta,n}^{\text{meas,H}}[k]\hat{\underline{H}}_{s_\eta,n}^{\text{dipole}}[k]e^{j\alpha_\eta[k]} - \hat{\underline{H}}_{s_\eta,n}^{\text{dipole,H}}[k]\hat{\underline{H}}_{s_\eta,n}^{\text{dipole}}[k]$$
$$\overset{!}{=} 0 \quad (43)$$

holds, where $\langle \cdot, \cdot \rangle$ denotes the complex scalar product and $(\cdot)^{\text{H}}$ denotes the conjugate transpose and must be satisfied by the real and imaginary parts. The imaginary part

$$\text{Im}\left\{ \hat{\underline{H}}_{s_\eta,n}^{\text{meas,H}}[k]\hat{\underline{H}}_{s_\eta,n}^{\text{dipole}}[k]e^{j\alpha_\eta[k]} \right\} \overset{!}{=} 0 \quad (44)$$

can only be solved by

$$\alpha_\eta[k] = \begin{cases} \alpha_{\eta,1}[k] = -\arg\left\{ \hat{\underline{H}}_{s_\eta,n}^{\text{meas,H}}[k]\hat{\underline{H}}_{s_\eta,n}^{\text{dipole}}[k] \right\} \\ \alpha_{\eta,2}[k] = \alpha_{\eta,1}[k] + \pi. \end{cases} \quad (45)$$

The real part yields

$$\text{Re}\left\{ \hat{\underline{H}}_{s_\eta,n}^{\text{meas,H}}[k]\hat{\underline{H}}_{s_\eta,n}^{\text{dipole}}[k]e^{j\alpha_\eta[k]} \right\}$$
$$= \hat{\underline{H}}_{s_\eta,n}^{\text{dipole,H}}[k]\hat{\underline{H}}_{s_\eta,n}^{\text{dipole}}[k] \geq 0. \quad (46)$$

Inserting

$$\left| \hat{\underline{H}}_{s_\eta,n}^{\text{meas,H}}[k]\hat{\underline{H}}_{s_\eta,n}^{\text{dipole}}[k] \right| e^{j\arg\left\{ \hat{\underline{H}}_{s_\eta,n}^{\text{meas,H}}[k]\hat{\underline{H}}_{s_\eta,n}^{\text{dipole}}[k] \right\}} e^{j\alpha_\eta[k]}$$
$$= \left| \hat{\underline{H}}_{s_\eta,n}^{\text{meas,H}}[k]\hat{\underline{H}}_{s_\eta,n}^{\text{dipole}}[k] \right| \cdot \begin{cases} 1 & \text{for } \alpha_{\eta,1}[k] \\ -1 & \text{for } \alpha_{\eta,2}[k] \end{cases} \quad (47)$$

into (46) only yields $\alpha_{\eta,1}[k]$ as a valid solution for (43).

References

[1] M. Vossiek, L. Wiebking, P. Gulden, J. Wieghardt, C. Hoffmann, and P. Heide, "Wireless local positioning," *IEEE Microw. Mag.*, vol. 4, no. 4, pp. 77–86, Dec. 2003.

[2] H. Liu, H. Darabi, P. Banerjee, and J. Liu, "Survey of wireless indoor positioning techniques and systems," *IEEE Trans. Syst., Man, Cybern. C, Appl. Rev.*, vol. 37, no. 6, pp. 1067–1080, Nov. 2007.

[3] V. Pasku *et al.*, "Magnetic field-based positioning systems," *IEEE Commun. Surveys Tuts.*, vol. 19, no. 3, pp. 2003–2017, 3rd Quart., 2017.

[4] C. Medina, J. C. Segura, and A. De la Torre, "Ultrasound indoor positioning system based on a low-power wireless sensor network providing sub-centimeter accuracy," *Sensors*, vol. 13, no. 3, pp. 3501–3526, 2013. [Online]. Available: http://www.mdpi.com/1424-8220/13/3/3501

[5] H. Hile and G. Borriello, "Positioning and orientation in indoor environments using camera phones," *IEEE Comput. Graph. Appl.*, vol. 28, no. 4, pp. 32–39, Jul. 2008.

[6] S. Grzonka, G. Grisetti, and W. Burgard, "A fully autonomous indoor quadrotor," *IEEE Trans. Robot.*, vol. 28, no. 1, pp. 90–100, Feb. 2012.

[7] S. He and S.-H. G. Chan, "Wi-Fi fingerprint-based indoor positioning: Recent advances and comparisons," *IEEE Commun. Surveys Tuts.*, vol. 18, no. 1, pp. 466–490, 1st Quart., 2015.

[8] S. Schwarzer, M. Vossiek, M. Pichler, and A. Stelzer, "Precise distance measurement with IEEE 802.15.4 (ZigBee) devices," in *Proc. IEEE Radio Wireless Symp.*, Jan. 2008, pp. 779–782.

[9] R. Faragher and R. Harle, "Location fingerprinting with Bluetooth low energy beacons," *IEEE J. Sel. Areas Commun.*, vol. 33, no. 11, pp. 2418–2428, Nov. 2015.

[10] S. Gezici *et al.*, "Localization via ultra-wideband radios: A look at positioning aspects for future sensor networks," *IEEE Signal Process. Mag.*, vol. 22, no. 4, pp. 70–84, Jul. 2005.

[11] J. A. del Peral-Rosado, R. Raulefs, J. A. López-Salcedo, and G. Seco-Granados, "Survey of cellular mobile radio localization methods: From 1G to 5G," *IEEE Commun. Surveys Tuts.*, vol. 20, no. 2, pp. 1124–1148, 2nd Quart., 2017.

[12] H. Wang, G. Bauer, F. Kirsch, and M. Vossiek, "Hybrid RFID system-based pedestrian localization: A case study," in *Proc. 10th Workshop Positioning, Navigat. Commun. (WPNC)*, Mar. 2013, pp. 1–6.

[13] J. Borenstein and L. Feng, "Measurement and correction of systematic odometry errors in mobile robots," *IEEE Trans. Robot. Autom.*, vol. 12, no. 6, pp. 869–880, Dec. 1996.

[14] A. R. J. Ruiz, F. S. Granja, J. C. P. Honorato, and J. I. G. Rosas, "Accurate pedestrian indoor navigation by tightly coupling foot-mounted IMU and RFID measurements," *IEEE Trans. Instrum. Meas.*, vol. 61, no. 1, pp. 178–189, Jan. 2012.

[15] N. El-Sheimy and X. Niu, "The promise of MEMS to the navigation community," *Inside GNSS*, vol. 2, no. 2, pp. 46–56, 2007.

[16] D. D. Arumugam, J. D. Griffin, D. D. Stancil, and D. S. Ricketts, "Experimental study on the effects of groups of people on magneto-quasistatic positioning accuracy," in *Proc. IEEE Int. Symp. Antennas Propag.*, Jul. 2018, pp. 1–2.

[17] B. Gozick, K. P. Subbu, R. Dantu, and T. Maeshiro, "Magnetic maps for indoor navigation," *IEEE Trans. Instrum. Meas.*, vol. 60, no. 12, pp. 3883–3891, Dec. 2011.

[18] X. Wang, M. Q.-H. Meng, and C. Hu, "A localization method using 3-axis magnetoresistive sensors for tracking of capsule endoscope," in *Proc. Int. Conf. IEEE Eng. Med. Biol. Soc.*, Aug. 2006, pp. 2522–2525.

[19] Z. Kasmi, A. Norrdine, and J. Blankenbach, "Towards a decentralized magnetic indoor positioning system," *Sensors*, vol. 15, no. 12, pp. 30319–30339, 2015. [Online]. Available: http://www.mdpi.com/1424-8220/15/12/29799

[20] G. de Angelis, A. de Angelis, V. Pasku, A. Moschitta, and P. Carbone, "An experimental system for tightly coupled integration of GPS and AC magnetic positioning," *IEEE Trans. Instrum. Meas.*, vol. 65, no. 5, pp. 1232–1241, May 2016.

[21] T. E. Abrudan, Z. Xiao, A. Markham, and N. Trigoni, "Distortion rejecting magneto-inductive three-dimensional localization (MagLoc)," *IEEE J. Sel. Areas Commun.*, vol. 33, no. 11, pp. 2404–2417, Nov. 2015.

[22] V. Pasku *et al.*, "A magnetic ranging-aided dead-reckoning positioning system for pedestrian applications," *IEEE Trans. Instrum. Meas.*, vol. 66, no. 5, pp. 953–963, May 2017.

[23] A. Plotkin and E. Paperno, "3-D magnetic tracking of a single subminiature coil with a large 2-D array of uniaxial transmitters," *IEEE Trans. Magn.*, vol. 39, no. 5, pp. 3295–3297, Sep. 2003.

[24] D. D. Arumugam, J. D. Griffin, D. D. Stancil, and D. S. Ricketts, "Three-dimensional position and orientation measurements using magneto-quasistatic fields and complex image theory [measurements corner]," *IEEE Antennas Propag. Mag.*, vol. 56, no. 1, pp. 160–173, Feb. 2014.

[25] G. de Angelis *et al.*, "An indoor AC magnetic positioning system," *IEEE Trans. Instrum. Meas.*, vol. 64, no. 5, pp. 1267–1275, May 2015.

[26] V. Pasku, A. de Angelis, M. Dionigi, G. de Angelis, A. Moschitta, and P. Carbone, "A positioning system based on low-frequency magnetic fields," *IEEE Trans. Ind. Electron.*, vol. 63, no. 4, pp. 2457–2468, Apr. 2016.

[27] G. de Angelis, A. de Angelis, A. Moschitta, and P. Carbone, "Comparison of measurement models for 3D magnetic localization and tracking," *Sensors*, vol. 17, no. 11, p. 2527, 2017. [Online]. Available: http://www.mdpi.com/1424-8220/17/11/2527

[28] F. H. Raab, "Quasi-static magnetic-field technique for determining position and orientation," *IEEE Trans. Geosci. Remote Sens.*, vol. GRS-19, no. 4, pp. 235–243, Oct. 1981.

[29] C. Hu, S. Song, X. Wang, M. Q.-H. Meng, and B. Li, "A novel positioning and orientation system based on three-axis magnetic coils," *IEEE Trans. Magn.*, vol. 48, no. 7, pp. 2211–2219, Jul. 2012.

[30] A. Sheinker, B. Ginzburg, N. Salomonski, L. Frumkis, and B.-Z. Kaplan, "Localization in 3-D using beacons of low frequency magnetic field," *IEEE Trans. Instrum. Meas.*, vol. 62, no. 12, pp. 3194–3201, Dec. 2013.

[31] V. Pasku, A. de Angelis, G. de Angelis, A. Moschitta, and P. Carbone, "Magnetic field analysis for 3-D positioning applications," *IEEE Trans. Instrum. Meas.*, vol. 66, no. 5, pp. 935–943, May 2017.

[32] J. D. Jackson, *Classical Electrodynamics*, 3rd ed. Hoboken, NJ, USA: Wiley, 1962.

[33] M. Dionigi, G. De Angelis, A. Moschitta, M. Mongiardo, and P. Carbone, "A simple ranging system based on mutually coupled resonating circuits," *IEEE Trans. Instrum. Meas.*, vol. 63, no. 5, pp. 1215–1223, May 2014.

[34] M. Hehn, M. Vossiek, F. Dollinger, K. Leo, B. Kheradmand-Boroujeni, and F. Ellinger, "Optimized coil design for magnetic local positioning systems," in *Proc. 11th German Microw. Conf. (GeMiC)*, Mar. 2018, pp. 383–386.

[35] B. Hesterman, "Analysis and modeling of magnetic coupling," *IEEE Power Electron. Soc.*, 2007.

[36] D. Titterton, J. L. Weston, and J. Weston, *Strapdown Inertial Navigation Technology*. Stevenage, U.K.: IET, 2004.

[37] T. M. Cover and J. A. Thomas, *Elements of Information Theory*. Hoboken, NJ, USA: Wiley, 2012.

[38] T. K. Moon and W. C. Stirling, *Mathematical Methods and Algorithms for Signal Processing*. Upper Saddle River, NJ, USA: Prentice-Hall, 2000.

Erik Sippel was born in Fürth, Germany, in 1991. He received the M.Sc. degree in electronic engineering from Friedrich-Alexander-Universität Erlangen-Nürnberg (FAU), Erlangen, Germany, in 2015, where he is currently pursuing the Ph.D. degree.

In 2016, he joined the Institute of Microwaves and Photonics, FAU. His current research interests include indoor localization, especially radar for near-field localization, data transmission, and analog-to-digital conversion.

Christian Carlowitz (S'13–M'17) was born in Wolfenbüttel, Germany, in 1985. He received the Dipl.-Ing. degree in information technology from the Clausthal University of Technology, Clausthal-Zellerfeld, Germany, in 2010, and the Dr.-Ing. degree from Friedrich-Alexander-Universität Erlangen-Nürnberg (FAU), Erlangen, Germany, in 2018. His Dr.-Ing. thesis was focused on wireless high-speed communication based on regenerative sampling.

He is currently with the Institute of Microwaves and Photonics, FAU, where he is leading the Microwave and Photonic Systems Group since 2018. His current research interests include conception, design, and implementation of innovative system architectures for radar and communication frontends at microwave, mm-wave, and optical frequencies, especially in hardware concepts as well as analog and digital signal processing techniques for ultrawideband high-speed communication systems, full-duplex mobile communication transceivers, massive multiple-in multiple-out base stations, and for ranging and communication with mm-wave radio-frequency identification systems.

Dr. Carlowitz is member of the IEEE Microwave Theory and Techniques Society (MTT-S) and serves as a member for the IEEE MTT-S Technical Coordinating Committee Digital Signal Processing (MTT-9). He is a regular reviewer of the IEEE TRANSACTIONS ON MICROWAVE THEORY AND TECHNIQUES as well as of several international MTTS-sponsored conferences including EuMW, ICMIM, and GeMiC.

Martin Vossiek (M'96–SM'05–F'16) received the Ph.D. degree from Ruhr University Bochum, Bochum, Germany, in 1996.

In 1996, he joined Siemens Corporate Technology, Munich, Germany, where he was the Head of the Microwave Systems Group from 2000 to 2003. Since 2003, he has been a Full Professor with Clausthal University of Technology, Clausthal-Zellerfeld, Germany. Since 2011, he has been the Chair of the Institute of Microwaves and Photonics, Friedrich-Alexander-Universität Erlangen-Nürnberg, Erlangen, Germany. He has authored or coauthored more than 200 papers. His holds more than 90 granted patents. His current research interests include radar, transponder, RF identification, communication, and locating systems.

Dr. Vossiek has been a member of organizing committees and Technical Program Committees for many international conferences. He is a member of the German IEEE Microwave Theory and Techniques (MTT)/Antennas and Propagation Chapter Executive Board and Microwave Systems Subcommittee MTT-16. He was the Founding Chair of the MTT IEEE Technical Coordinating Subcommittee MTT-27 Wireless-Enabled Automotive and Vehicular Application. He was a recipient of several international awards. He has served on the Review Boards for numerous technical journals. Since 2013, he has been an Associate Editor of the IEEE TRANSACTIONS ON MICROWAVE THEORY AND TECHNIQUES.

Markus Hehn (S'17) was born in Bamberg, Germany, in 1987. He received the M.Sc. degree in electrical engineering from Friedrich-Alexander-Universität Erlangen-Nürnberg (FAU), Erlangen, Germany, in 2016, where he is currently pursuing the Ph.D. degree.

In 2016, he joined the Institute of Microwaves and Photonics, FAU. His current research interests include radar for near-field localization and localization systems for indoor environment.